[17] T. Alves, B. Poussot, and J. M. Laheurte, "Analytical propagation modeling of BAN channels based on the creeping-wave theory," *IEEE Trans. Antennas Propag.*, vol. 59, pp. 1269–1274, 2011.
[18] K. Li and Y. L. Lu, "Electromagnetic field from a horizontal electric dipole in the spherical electrically earth coated with n-layered dielectrics," *Progr. Electromagn. Res., PIER*, vol. 54, pp. 221–244, 2005.
[19] R. W. P. King, G. J. Fikioris, and R. B. Mack, *Cylindrical Antennas and Arrays*. Cambridge, U.K.: Cambridge Univ. Press, 2002, Ch. 8 and 9.
[20] C. A. Balanis, *Advanced Engineering Electromagnetics*. New York, NY, USA: Wiley, 1989.
[21] A. R. Guraliuc *et al.*, "Effect of textile on the propagation along the body at 60 GHz," *IEEE Trans. Antennas Propag.*, vol. 62, no. 3, pp. 1489–1494, Mar. 2014.
[22] K. A. Norton, "The physical reality of space and surface waves in the radiation field of radio antennas," *Proc. Inst. Radio Eng.*, vol. 25, no. 9, pp. 1192–1202, 1937.

Flexible Antenna Integrated With an Epitaxial Lift-Off Solar Cell Array for Flapping-Wing Robots

Jungsuek Oh, Kyusang Lee, Tyler Hughes, Stephen Forrest, and Kamal Sarabandi

***Abstract*—We describe the integration of a flexible UHF antenna with an epitaxial lift-off thin-film III-V solar cell array used for power generation and wireless communication in a flapping-wing robotic platform. The antenna is configured to utilize the cells and their interconnections as a part of the radiating element, leading to compact multifunctional antenna/solar cell array surface. The high junction capacitance of individual solar cells allows RF current conduction through the cells without an associated power penalty. Metallic interconnects in the solar cell array carry both the DC power as well as forming part of the UHF antenna. To suppress RF current leakage into the DC circuit used for conducting the solar cell current, a RF choke is inserted between the antenna and the solar cells in the DC path. The performance characteristics of the integrated antenna and solar cell array verify the predicted performance of the antenna for reliable communication. Further, mounting the thin film solar cell array on a $25\ \mu$m thick Kapton sheet is shown to be a robust power source when positioned on the flexible wings of flapping robotic platforms. Details about design procedure and performance of the proposed integrated antenna are discussed.**

***Index Terms*—Conformal antennas, robots, solar power generation.**

I. Introduction

Rapid developments in thin film optoelectronic devices have accelerated the application of flexible electronics, propelled by the increasing demand for lighter and smaller products with low power consumption [1], [2]. Twistable and foldable devices promise new functionality for many applications in areas such as communication, displays, and health care [3], [4]. For example, a user with a flexible mobile phone may only need to twist the appliance to dismiss a call, change a program, etc. [3]. Foldable devices such as flexible keyboards and displays can provide portability and save space when not in operation [4]. In this context, flexible antennas also address a wide range of applications in wireless communication when they are integrated with conformal electronics platforms [5]–[7].

Here, we demonstrate that such flexible electronics can be applied to micro-unmanned autonomous robots that have significant demands for small size, weight, and power (SWaP). Such systems often require a power supply that is sufficient to complete a mission, which may be realized using an array of photovoltaic cells [8]. This can be accomplished by covering the exposed upper surfaces of robotic flyers with light-weight, thin and flexible solar cells. The SWaP requirements can also be efficiently met by including multi-functionality among different system components. For example, such robots often need wireless transceivers operating at ultrahigh frequencies (UHF). Hence, multi-functionality is achieved by integrating the UHF antenna with the solar cells on the robot wing. Early studies regarding the integration of antennas with solar cells concentrated on stacking the two components in efficient ways, considering the two components as physically separated parts [9]–[11]. Recently, efforts to utilize solar cells as radiating elements for size reduction in the integrated structure have been reported [12], [13]. However, the integrated packages that consist of brittle and heavy solar cells are too bulky to be practical for robotic flappers.

Here, we address design/fabrication/integration issues for all-flexible solar antenna on the wings and its topology for bendable and tolerant flapping wings and efficient area utilization. A conformal planar antenna integrated with a flexible, durable and light weight thin film GaAs solar cells mounted on a wing of a flapping robot is presented. The solar cells were prepared by an epitaxial lift-off (ELO) process that enables the separation of thin-film single-crystal layers from the parent substrate [14]–[17]. The UHF antenna is designed to allow for the placement of centimeter-size solar cells in series with metallic traces of the antenna. The antenna operates with both RF and DC signals, and its performance is unaffected by the rectifying solar cell. Further, the integrated circuit does not limit the motion of the robot wings. Antenna impedance and radiation characteristics are found to be comparable to those of a similarly configured discrete component.

This communication is organized as follows: Section II describes the configuration of the integrated circuits. Section III presents the fabrication process used for integration. Finally, in Section IV we discuss the simulated and measured antenna impedance under different bending conditions.

II. Configuration of Flexible Antenna and Solar Cell Array on a Flapping-Wing Robot

Flapping wings that propel the miniature robotic flyer have a large area surface that can be exposed to solar radiation. Hence, they provide a platform for mounting photovoltaic cells that can supply energy as long as the embedded electronics present an acceptably small load on the flapper itself. Whole integrated circuit consists of a flexible antenna incorporating solar cell array and a spiral RF choke. Fig. 1(a) and (b) show RF and DC current paths indicating what solar cells are related to the two current paths. It should be noted that the RF current path is designed to exhibit the geometry of meander dipole antenna loaded by RF choke (inductor). In order to minimize effects of metallic robot body on

Manuscript received August 01, 2013; revised December 30, 2013; accepted May 01, 2014. Date of publication May 09, 2014; date of current version July 31, 2014. This work was supported in part by the U.S. Army Research Laboratory under contract W911NF and prepared through collaborative participation in the Microelectronics Center of Micro Autonomous Systems and Technology (MAST) Collaborative Technology Alliance (CTA) and NSF under contract ECCS 1101868.

J. Oh and K. Sarabandi are with the Radiation Laboratory, Department of Electrical Engineering and Computer Science, The University of Michigan at Ann Arbor, Ann Arbor, MI 48109-2122 USA (e-mail: jungsuek@umich.edu; saraband@eecs.umich.edu).

K. Lee, T. W. Hughes, and S. Forrest are with the Optoelectronic Components and Materials Laboratory, Department of Electrical Engineering and Computer Science, and Physics, The University of Michigan at Ann Arbor, Ann Arbor, MI 48109-2122 USA (e-mail: kyusang@umich.edu; stevefor@umich.edu).

Color versions of one or more of the figures in this communication are available online at http://ieeexplore.ieee.org.

Digital Object Identifier 10.1109/TAP.2014.2322895

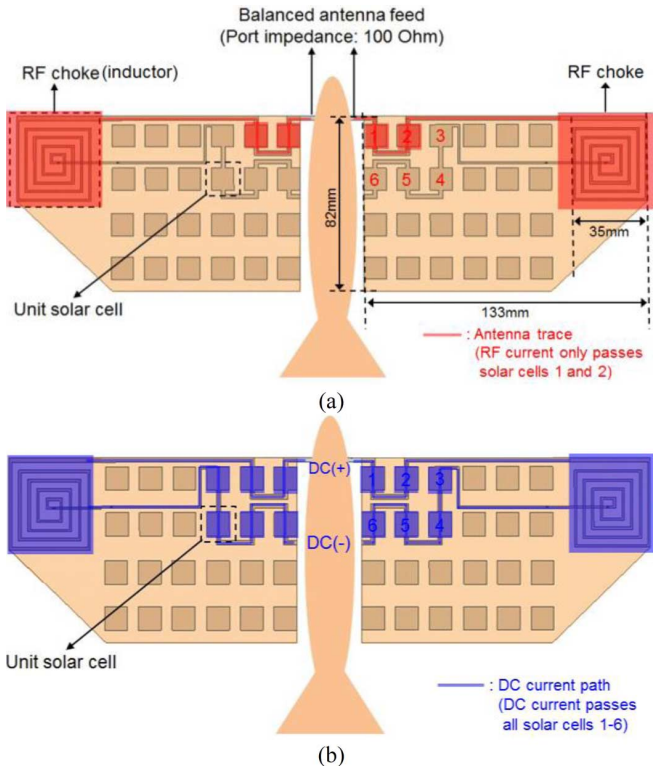

Fig. 1. (a) RF current path exhibiting antenna geometry loaded by RF choke (inductor) at the end of the antenna and (b) DC current path.

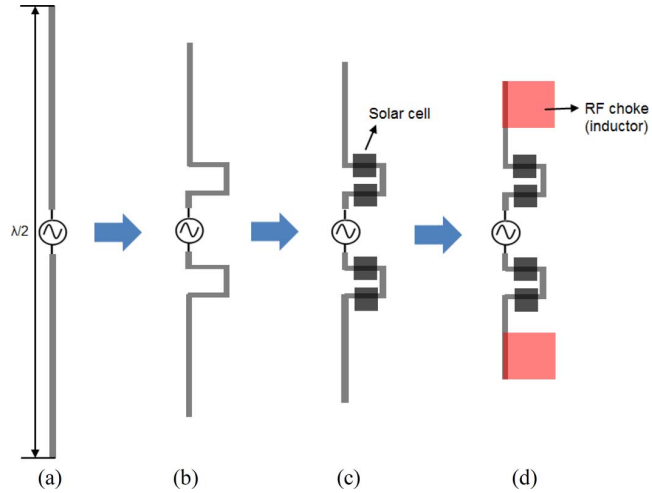

Fig. 2. (a) $\lambda/2$ dipole antenna (b) meander dipole antenna due to limited area on the wing, (c) meander dipole antenna including solar cells where solar cells are a radiating part of antenna geometry and (d) final meander solar dipole antenna loaded by RF choke (inductor).

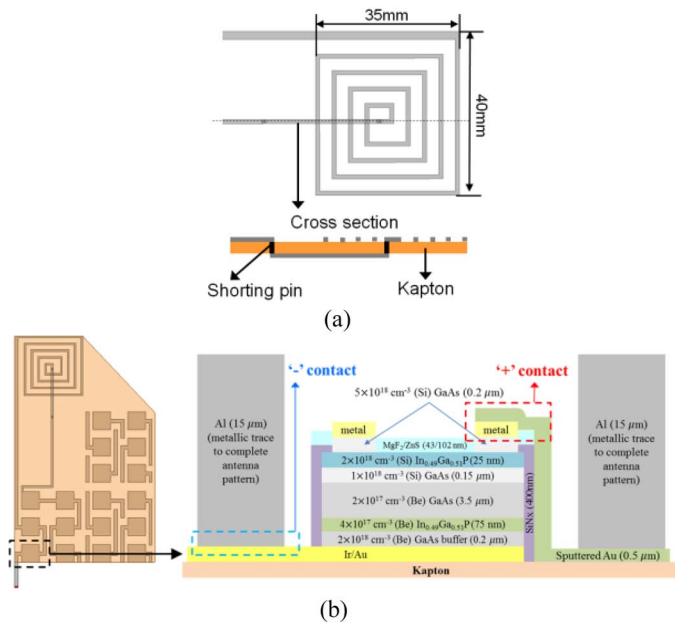

Fig. 3. (a) RF choke design and (b) cross-sectional schematic of the solar cell structure connected to antenna metallic trace. Dopant species (in parentheses), concentrations and thicknesses are shown for each layer.

the performance of antenna integrated in the wings, balanced architecture of dipole antenna that can form a zero potential plane where robot body is positioned is chosen. In addition, using RF choke, RF current is confined only into the antenna geometry and does not couple to the DC path returning to robot body (please note that Fig. 1(a) shows there is no RF current in '3', '4', '5' and '6' areas of blue trace in Fig. 1(b)). Without the RF choke, some current distributions induced on antenna trace and all solar cells can be out-of-phase hampering the realization of intended current distribution for $\lambda/2$ dipole antenna. This can cause the decrease in antenna performance.

Fig. 2 depicts each step in antenna design procedure starting from the conventional $\lambda/2$ dipole antenna. Finally, similar to the conventional dipole antenna, two antenna traces coming from the wings are connected to two differential outputs of RF transceiver in robot body, respectively. As discussed in Section IV, the thin-film solar cell capacitance conducts the RF current and introduces a small phase shift similar to that incurred in a similar circuit configuration. Fig. 3(a) shows the top and side views of the RF choke with vertical pins connecting the conductor in the center of the spiral to one on the reverse side of the thin substrate web. The top and lower metallic conductors are then connected to DC output pads. Fig. 3(b) shows a cross-sectional view of an epitaxial lift-off solar cell bonded to the Kapton sheet. In robot body, the antenna feed where both RF and DC current exist is split to two current paths. One is connected to RF module through DC block and the other is connected to battery through RF chock.

III. Fabrication

To maximize power generation from a limited area, a single crystalline III-V compound semiconductor solar cell is employed. The fabrication of single GaAs thin film solar cells has been discussed previously [14]; however, to develop a solar cell array, the wire bonding technology was developed to be compatible with the thin film devices. Therefore, previous thin film GaAs solar cell fabrication techniques were modified to include an interconnection that enables the integration of all components on a thin, flexible plastic substrate.

The solar cell structure is grown using gas source molecular beam epitaxy followed by transfer to a flexible plastic substrate via pressure cold welding to the Kapton substrate [14]. The heavy and brittle substrate is then removed by epitaxial lift off (ELO) [11], leaving behind only the thin and lightweight GaAs solar cell active region. The transferred thin film is next fabricated into solar cells and connected in series to supply power to the robot. Finally, the antenna and RF choke are patterned using vacuum thermal evaporation of Au through a shadow mask.

A 0.2 μm thick, Be-doped GaAs buffer layer is grown on a Zn-doped (100) GaAs wafer, followed by a 40 nm thick undoped AlAs sacrificial layer. The layer thicknesses and doping of each layer of the full epitaxial layer structure is shown in Fig. 3(b). A 5 nm thick Iridium

(Ir) adhesion layer is sputtered at 8.5 mTorr base pressure on a $50\ \mu\mathrm{m}$ thick Kapton sheet. Then a $1\ \mu\mathrm{m}$ thick Au layer is deposited on both the Kapton and the epitaxial layer surface using electron beam deposition. These two surfaces are then bonded by cold-welding by applying pressure to the structure with the two Au layers are in contact. The epitaxial layers are then lifted off by etching the sacrificial layer in a 10% HF solution.

Solar cell fabrication consists of deposition of a $\mathrm{Ni}(5\ \mathrm{nm})/\mathrm{Ge}(50\ \mathrm{nm})/\mathrm{Au}(0.8\ \mu\mathrm{m})$ grid onto the n-type surface by e-beam evaporation, and then patterned using photolithography and lift-off. The $(1\ \mathrm{cm})^2$ solar cell mesas are defined using photolithography and wet-etching of the GaAs active layer. Then, Au is wet-etched (TFA etchant, Transene CO) [12], followed by an Ir inductive coupled plasma etch using 9 sccm of Cl_2 gas at 4 mTorr for 9 sec to pattern the back-side metal array interconnects. The contacts are annealed for 1 hr at $180^{\circ}\mathrm{C}$. The top GaAs layer that lies outside the metal contact area is removed by wet etching. The conventional wire bonding technology, which uses heat, pressure and ultrasonic energy, is incompatible with plastic substrate mounting due to the substrate softness and low tolerance to elevated temperatures. To alleviate this problem, we employed metal sputtering to deposit interconnections, enabling conformal coating through passivated sidewalls combined with patterned rear side metal connection, which is described above. To allow for series connection of the solar cells, the sides of each solar cell are passivated using a 400 nm $\mathrm{SiN_x}$ layer deposited by plasma enhanced chemical vapor deposition and patterned by photolithography and plasma etching. After a $\mathrm{ZnS}(43\ \mathrm{nm})/\mathrm{MgF}_2(102\ \mathrm{nm})$ antireflective coating is deposited by e-beam evaporation, solar cells are connected in series using a $0.5\ \mu\mathrm{m}$ thick Au layer sputtered through a shadow-mask. This technique provides a robust thin film interconnection for the integration of multiple components on a flexible plastic substrate.

After solar cell fabrication, a $15\ \mu\mathrm{m}$ thick Al layer is deposited using a shadow mask and e-beam evaporation to form the antenna and RF choke. Then, the DC output metal connection is evaporated onto the reverse side of the Kapton sheet and connected to both the center of the RF choke and the contact pad on front side. Fig. 4 shows the antenna integrated with the solar cells and the RF choke. Considering the fact that the skin depth of Al at 350 MHz is about 4 um, the thickness og Al layer is chosen to be 15 um ($>$ 3 skin depth) to ensure high antenna efficiency.

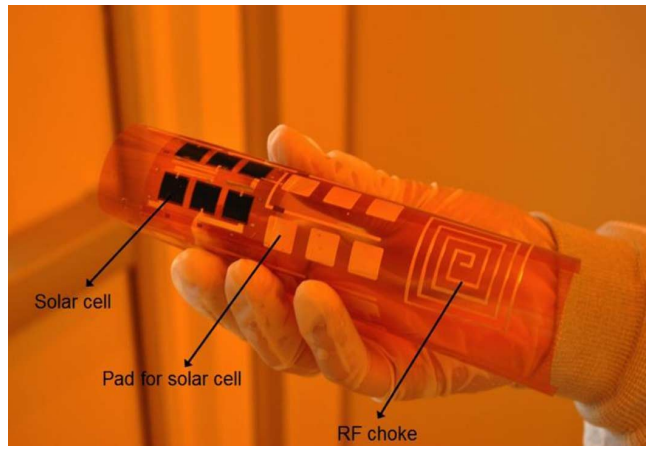

Fig. 4. Flexible antenna and solar cell array on a Kapton sheet.

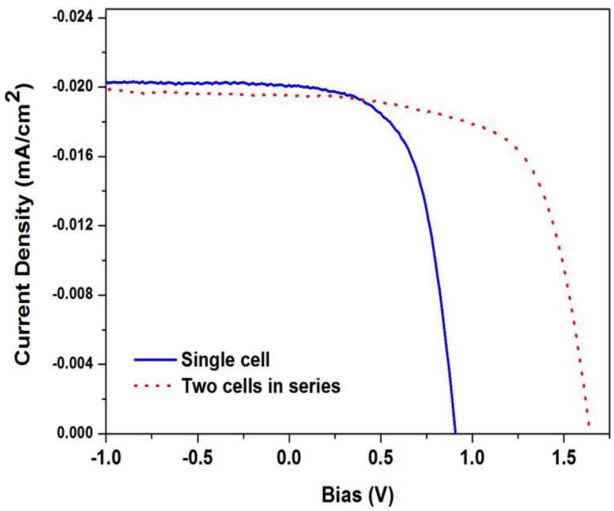

Fig. 5. Current density-voltage characteristic of a discrete solar cell and two solar cells in series.

IV. Measurement

A. Characteristics of Thin-Film Solar Cells

To demonstrate the effectiveness of power generation and the multi-functionality of device, the current density-voltage $(J-V)$ characteristics of the GaAs photovoltaic cell and a series array of two cells measured under simulated AM1.5G spectrum, 1 sun intensity $(100\ \mathrm{mW/cm^2})$ illumination are shown in Fig. 5. The optical power intensity is calibrated using a National Renewable Energy Laboratory certified Si reference photovoltaic cell. The cell short circuit current density is $19.5 \pm 0.6\ \mathrm{mA/cm^2}$ and the open circuit voltage is 0.90 ± 0.01 V with a fill factor of $55 \pm 4\ \%$ resulting in a power conversion efficiency of $10 \pm 1\ \%$. The short circuit current density for the array is $19.4\ \mathrm{mA/cm^2}$ and the open circuit voltage is 1.64 V with a fill factor of 64%.

B. Impedance Characteristics of Thin-Film Solar Cells

To employ the thin-film solar cell as a part of an efficient antenna, the effect of the solar cell on the RF antenna characteristics must be quantified. The input impedance of the $1\ \mathrm{cm^2}$ solar cell is measured with a vector network analyzer, where the contacts (see Fig. 3(b)) are connected by wire bonds to signal and ground. Using the measured S_{11}, the real and imaginary parts of the input impedance (Z_{in}) of the solar cell are calculated under illumination and in the dark. Fig. 6(a) and (b) indicate that the AC impedance is unaffected by illumination. As frequency increases, imaginary part of Z_{in} approaches zero. An additional measurement in broader frequency range of 0 to 10 MHz indicates that real part of Z_{in} also approaches zero very gradually (This measurement result is not shown here due to limited pages). This suggests that the solar cell acts as an AC short due to its high junction capacitance.

C. Antenna Characteristics

As shown in Fig. 1, the antenna allows conduction of the RF current through the thin-film solar cells. Due to the series configuration of the cells, the antenna geometry on two wings resembles a meander dipole loaded by RF chokes at the end. The RF chokes stop the flow of RF current while allowing the conduction of the DC current to be used for powering other functions of the robot. Input impedance of the whole meander solar dipole antenna can be predicted by testing monopole version of the antenna on large ground plane based on well-known fact that input impedance of monopole antenna on a large enough ground plane ($> \lambda/2$ where λ is the free-space wavelength) is half of that of

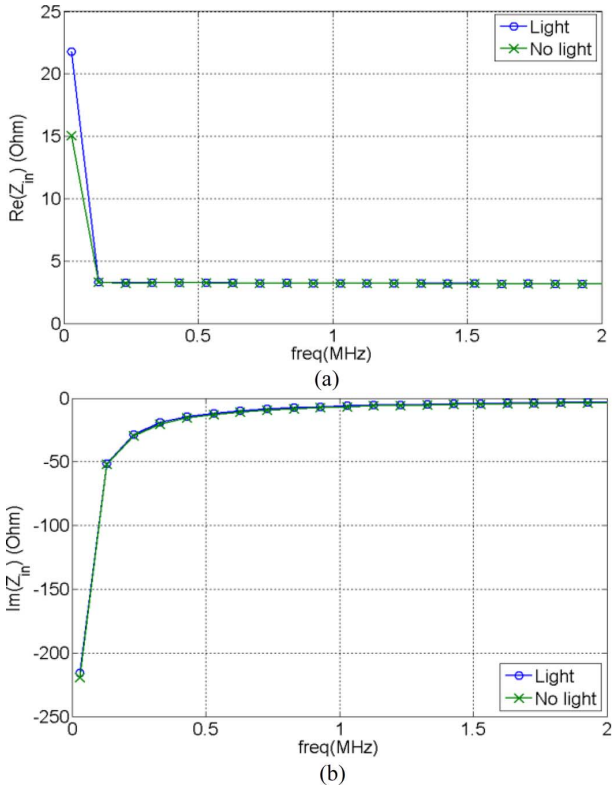

Fig. 6. Measured (a) real and (b) imaginary parts of the input impedance (Z_{in}) of the thin-film solar cell in the presence/absence of illumination.

dipole antenna. Here, 100 Ω and 50 Ω are used as source impedances of the dipole and monopole antennas, respectively. In addition, the use of a large ground plane ($600\ \mathrm{mm} \times 600\ \mathrm{mm}$) for the monopole is equivalent to a potential null surface existing between two arms of the actual dipole version. A balanced feed for dipole antennas produces a null surface in the plane bisecting the dipole structure. In this plane, any metallic structure like the antenna feed can be inserted without affecting the antenna characteristics. Therefore, in flapping robotic platforms, positioning components in the middle of two arms of the meander dipole antenna does not affect the performance of the antenna [18]–[21].

Since each thin-film solar cell is the AC equivalent to a metallic pad with the same dimension as the solar cell, the length of one arm of the dipole is adjusted so that the total current path length is $\sim \lambda_0/4$, where λ_0 is the free-space wavelength at the antenna operating frequency. We assume that the effect of the thin ($50\ \mu\mathrm{m}$) Kapton sheet can be ignored at the operating frequency (350 MHz). To determine the junction capacitance of the thin-film solar cell, the areas occupied by the solar cells are replaced with gold pads. The simulated S_{11} using Ansoft HFSS 13.0 is compared to the measured value of the antenna with solar cells under illumination, with results in Fig. 7. Agreement between measurement result with the solar cells and simulation result without solar cells but with the aforementioned gold pads indicates that the solar cells do not influence the RF antenna performance. Fig. 8 shows the measured S_{11} of the integrated solar cells and UHF antenna under illumination and in the dark. Apparently, the RF performance of the antenna is also unaffected by illumination. 10 dB return loss bandwidth of about 7% is observed from measured S_{11} in Figs. 7 and 8.

To test the RF choke operation, one of the DC outputs is grounded. Fig. 9 shows that while this causes a small change in impedance matching, the antenna operating (resonant) frequency remains unaffected. The change in input impedance is due to the limited inductance

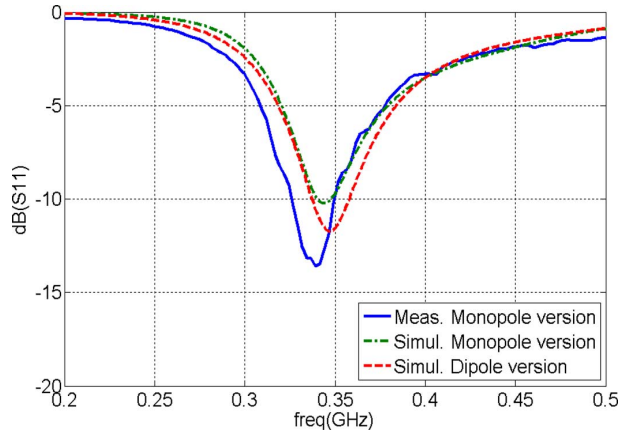

Fig. 7. Measured and simulated S_{11} parameter of the antenna under illumination.

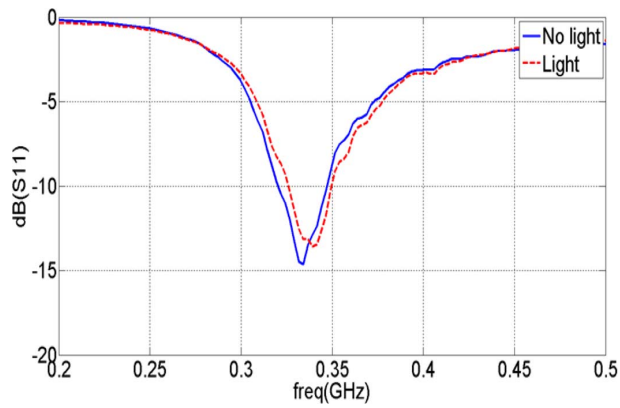

Fig. 8. Measured S_{11} under illumination and in the dark.

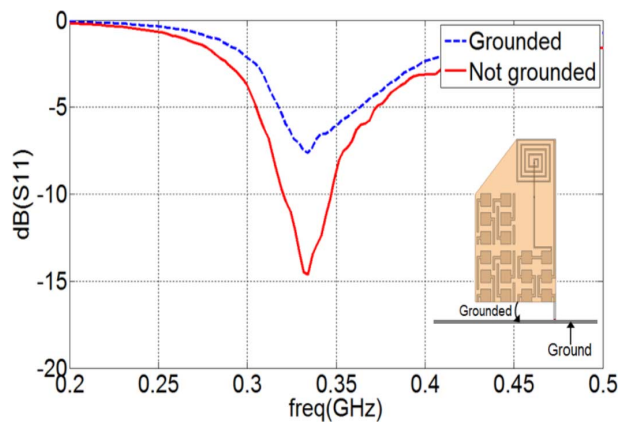

Fig. 9. Measured S_{11} for floating or connected DC output.

of the spiral inductor, and this change can be reduced by increasing the number of turns in the inductor. Fig. 10 shows current distribution in the antenna when one of the DC outputs is grounded. The RF current is confined over the antenna and RF choke, and does not couple to the DC path. Also, changes in S_{11} are measured under two bending conditions (see Fig. 11). The fabricated antenna is placed over Styrofoam cylinders with two different radii of curvature (8 cm and 11 cm). While the impedance is slightly changed due to varying parasitic coupling between the antenna and other metallic pathways on

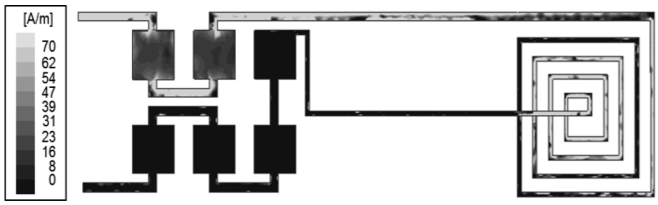

Fig. 10. Current distribution on the antenna when one DC output is grounded.

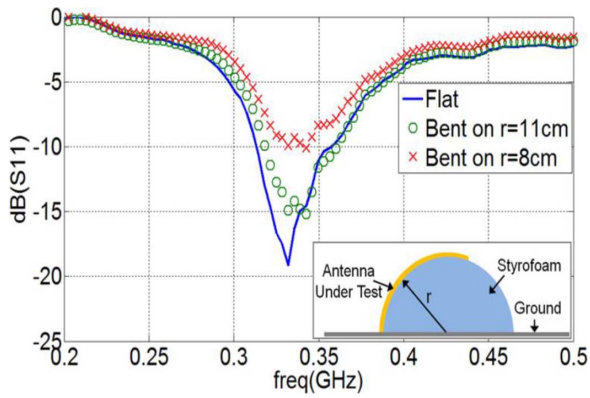

Fig. 11. Measured S_{11} for the antenna placed over Styrofoam cylinders with two different radii of curvatures (8 cm and 11 cm). The results are also compared to the flat case.

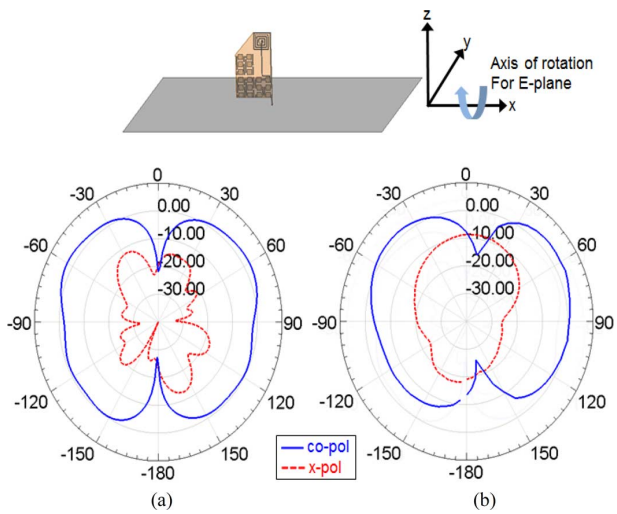

Fig. 12. (a) Simulated and (b) measured co- and cross-polarization (Gain_θ and Gain_θ) radiation patterns in the E (yz)–plane.

the solar cell array, changes in S_{11} are sufficiently small to allow for reliable communications. Finally, Fig. 12 indicates that the measured radiation pattern of the antenna agrees with the simulated radiation patterns, suggesting the operation of a monopole antenna with high efficiency of $\sim 90\%$. Measured and simulated gain are about 3 dBi, which is lower than typical gain of $\lambda/4$ monopole antenna on infinite ground plane due to miniaturized antenna size and finite ground plane. In addition, as expected, the ratio of co- to cross-polarized radiation in the azimuthal plane ($\theta = 90^\circ$), is relatively high (more than 10 dB).

V. Conclusion

A thin film antenna integrated with a flexible solar cell array suitable for communication and for supplying power to a flapping wing robot has been demonstrated. The thin-film solar cells with lateral dimensions of 1 cm are modeled as a capacitor that efficiently conducts the RF signal. The RF circuit properties are unaffected by illumination. The meander planar antenna incorporating the solar cells is integrated with a RF choke to allow for conduction of DC power while limiting the conduction of the RF signal. The performance of the antenna is tested under various bending conditions with minimal degradation to the antenna resonant frequency, return loss and solar cell power generation characteristics.

References

[1] A. Nathan, A. Ahnood, M. T. Cole, S. Lee, Y. Suzuki, P. Hiralal, F. Bonaccorso, T. Hasan, L. Garcia-Gancedo, A. Dyadyusha, S. Haque, P. Andrew, S. Hofmann, J. Moultrie, D. Chu, A. J. Flewitt, A. C. Ferrari, M. J. Kelly, J. Robertson, G. A. J. Amaratunga, and W. I. Milne, "Flexible electronics: The next ubiquitous platform," *Proc. IEEE*, vol. 100, pp. 1486–1517, 2012.

[2] C.-C. Tsai, "Recent development in flexible electronics," in *Proc. 16th Optoelectronics and Commun. Conf.*, 2011, pp. 370–371.

[3] P. Kodikara, (2011, Oct. 28)., Nokia Introduces The World's First Flexible Mobile phone., *Tech. Hamlet* [Online]. Available: http://tech-hamlet.com/2011/10/nokia-introduces-the-worlds-first-flexible-mobile-phone/

[4] S. Takamatsu, T. Imai, T. Yamashita, T. Kobayashi, K. Miyake, and T. Itoh, "Flexible fabric keyboard with conductive polymer-coated fibers," *IEEE Sensors*, pp. 659–662, 2011.

[5] A. C. Durgun and C. A. Balanis, "Design, simulation, fabrication and testing of flexible bow-tie antennas," *IEEE Trans. Antennas Propag.*, vol. 54, no. 12, Dec. 2011.

[6] S. H. Choi, T. J. Jung, and S. Lim, "Flexible antenna based on composite right/left-handed transmission line," *Electron. Lett.*, vol. 46, no. 17, Aug. 2010.

[7] H. R. Khaleel, H. M. Al-Rizzo, D. G. Rucker, and S. Mohan, "A compact polyimide-based UWB antenna for flexible electronics," *IEEE Antennas Wireless Propag. Lett.*, vol. 11, pp. 564–567, May 2012.

[8] C. Bendel, N. Henze, and J. Kirchhof, "Solar cell antennas in wireless communication and radio broadcast systems," presented at the 19th Eur. Photovoltaic Solar Energy Conf. and Exhibition, Paris, France, Jun. 2004.

[9] M. Tanaka, Y. Suzuki, K. Araki, and R. Susuki, "Microstrip antennas with solar cells for microsatellites," *Electron. Lett.*, vol. 31, no. 1, pp. 263–266, 1996.

[10] S. Vaccaro, J. R. Mosig, and P. Maagt, "Two advanced solar antenna SOLANT designs for satellite and terrestrial communications," *IEEE Trans. Antennas Propag.*, vol. 51, no. 8, pp. 2028–2034, 2003.

[11] W. Turpin and R. Baktur, "Meshed patch antennas integrated on solar cells," *IEEE Antennas Wireless Propag. Lett.*, vol. 8, pp. 693–696, 2009.

[12] N. Henze, C. Bendel, J. Kirchhof, and H. Früchting, "Application of photovoltaic solar cells in planar antenna structures," in *Proc. 12th Int. Conf. on Antennas and Propagation*, Exeter, U.K., Mar. 31-Apr. 1 2003, pp. 731–734.

[13] N. Henze, M. Weitz, P. Hofmann, C. Bendel, J. Kirchoff, and H. Fruchting, "Investigations on planar antennas with photovoltaic solar cells for mobile communications," in *Proc. IEEE Int. Symp. on Personal, Indoor and Mobile Radio Commun.*, 2004, vol. 1, pp. 622–626.

[14] Y. Eli, T. Gmitter, J. P. Harbison, and R. Bhat, "Extreme selectivity in the lift-off of epitaxial GaAs films," *Appl. Phys. Lett.*, vol. 51, 1987, 2222.

[15] L. Kyusang, S. Kuen-Ting, Z. D. Jeramy, R. K. Christopher, and F. R. Stephen, "Multiple growth of epitaxial lift-off solar cells from a single InP substrate," *Appl. Phys. Lett.*, vol. 97, 2010, 101107.

[16] L. Kyusang, Z. D. Jeramy, X. Xin, S. Kai, and F. R. Stephen, "Reuse of GaAs substrates for epitaxial lift-off by employing protection layers," *J. Appl. Phys.*, vol. 111, 2012, 033527.

[17] L. Kyusang, Z. D. Jeramy, Z. Yifan, and F. R. Stephen, "Epitaxial lift-off by GaAs thin film solar cells followed by substrate reuse," in *Proc. IEEE 38th Photovoltaic Specialists Conf.*, Jun. 3-8, 2012, pp. 1698–1700.

[18] J. Oh and K. Sarabandi, "Low profile, miniaturized, inductively coupled capacitively loaded monopole antenna," *IEEE Trans. Antennas Propag.*, vol. 60, pp. 1206–1213, Mar. 2012.

[19] W. S. Lee, H. S. Tae, K. S. Oh, and J. W. Yu, "A balanced-fed dual inverted-F antenna with reduced human body effects," Transl.: *Int. J. Antennas Propag.*, vol. 2013 [Online]. Available: http://www.hindawi.com/journals/ijap/2013/814375/

[20] J. Oh, J. Choi, F. T. Dagefu, and K. Sarabandi, "Extremely small two-element monopole antenna for HF band applications," *IEEE Trans. Antennas Propag.*, vol. 61, no. 6, pp. 2991–2999, Jun. 2013.
[21] J. Oh and K. Sarabandi, "Low profile vertically polarized omni-directional wideband antenna with capacitively coupled parasitic elements," *IEEE Trans. Antennas Propag.*, vol. 62, no. 2, pp. 977–982, Feb. 2014.

Parameterization of a Polarimetric Diffuse Scattering Model in Indoor Environments

Francesco Mani, Enrico M. Vitucci, François Quitin, Vittorio Degli-Esposti, and Claude Oestges

***Abstract*—Diffuse or dense multipath components play an important role in determining the polarization behavior of wireless transmission channels. In this communication, we parametrize a polarimetric diffuse scattering model in two indoor environments. Our method relies on the empirical extraction of dense multipaths by means of a high resolution algorithm and on the investigation of the properties of this diffuse component. The analysis reveals that diffuse scattering significantly depolarizes the impinging wave in indoor scenarios, yielding cross-polar discrimination values close to 0 dB.**

***Index Terms*—Indoor radio communications, polarization, propagation, ray tracing, scattering.**

I. Introduction

Diffuse scattering is a phenomenon which originates from the presence of random, distributed surface or volume irregularities in building walls or other kinds of obstacles. With respect to specular reflection, diffuse scattering produces a further spreading of the scattered power in non-specular directions and might represent a relevant part of the total received power in typical indoor environments, especially when a dominant, direct path is not present. It is taken into account in most recent ray-tracing (RT) tools through physics-based heuristic models such as the effective roughness (ER) model [1]. Thanks to this extension, RT models are capable of modeling the non-coherent, dense multipath component of wireless channels. As diffuse multipaths are non-coherent, their impact on MIMO systems must be accounted for, since they tend to lower multi-antenna correlations and increase MIMO channel ranks, and thus boost diversity and multiplexing gains. Furthermore, with the advent of polarized MIMO systems, diffuse scattering must also be characterized in the polarization domain, as initiated in [2]–[4]. The ER model has been shown in [1] to considerably improve the performance of RT tools, since it allows to model, in a statistical way, the surface and volume irregularities of building walls which cannot be included in the input databases. Moreover, such irregularities can have a strong impact on the depolarization of diffuse multipaths, as demonstrated in [5], [6].

For these reasons, a polarimetric version of the ER diffuse scattering model was derived and parameterized in [7] for outdoor environments. This was achieved by identifying diffuse scattered power reflected by homogeneous isolated buildings in wideband measured channel impulse responses. The derived model was further validated in more complex outdoor scenarios such as street canyons [8].

The parameterization of this polarimetric model is still missing for the indoor environments, and it is the objective of the present work. However, the approach used for single-building outdoor scenarios cannot be adopted for indoor environments, as it would be rather difficult to define and isolate representative surfaces and to identify diffuse paths. Hence, we resort to parameterize the diffuse scattering model by extracting the dense multipath component (DMC) from double-directional measurements using super-resolution estimation techniques. This method builds upon the empirical evidence that DMC can be interpreted as diffuse scattering and vice-versa [9].

The outline of the communication is as follows. In Section II, we recall the diffuse scattering model which needs to be parameterized. Section III details the measurement campaign and the DMC extraction procedure, whose outputs are then used in Section IV to derive the new model parameters. Section V presents the effects of diffused paths on global channel characteristics such as branch power ratios in multi-polarized settings. Finally, conclusions are drawn in Section VI.

II. Polarimetric Diffuse Scattering Model

The polarimetric properties of the DMC are investigated here adopting a diffuse scattering model based on the effective roughness (ER) approach [1]. For each wall-surface element, it is assumed that part of the impinging power is reflected specularly and part is scattered according to a given diffuse scattering coefficient S, which determines the amount of power scattered in all the directions at expenses of the specular reflection. Several shapes of the scattering patterns are possible, but in the present work, a directive lobe centered around the direction of specular reflection has been chosen, as this option gave the best results in terms of accuracy with respect to measurements [1]. This simple one-lobe scattering diagram is expressed by the following:

$$E_s = \left(\frac{S \cdot E_{i0}}{r_i \cdot r_s}\right) \sqrt{\frac{dS \cos\theta_i}{F_{\alpha_r}}} \left(\frac{1+\cos\psi_r}{2}\right)^{\frac{\alpha_r}{2}} \quad (1)$$

where E_{i0} is the amplitude of the incident field at unit distance from the Tx, r_i, r_s are the distances between the scattering point and Tx/Rx, respectively, $S \in [0,1]$ is a parameter which sets the amount of scattered power at the expenses of specular reflection, dS is the area of the wall element, θ_i is the incidence angle, ψ_r is the angle between the specular reflection direction and the scattering direction (θ_s, ϕ_s), the exponent α_r sets the width of the scattering lobe, and F_{α_r} is a parameter depending on α_r properly defined in order to satisfy the power balance [1].

Manuscript received September 23, 2013; revised April 30, 2014; accepted May 01, 2014. Date of publication May 09, 2014; date of current version July 31, 2014. This work was supported by European COST Action IC1004 on Cooperative Radio Communications for Green Smart Environments and was also carried out in the framework of the Network of Excellence in Wireless Communications NEWCOM#. The work of C. Oestges was supported by the Belgian Fonds de la Recherche Scientifique.

F. Mani is with the COMELEC Department, Telecom ParisTech, Paris, France (e-mail: Francesco.Mani@telecom-paristech.fr).

E. M. Vitucci and V. Degli-Esposti are with the University of Bologna, Dipartimento di Ingegneria dell'Energia Elettrica e dell'Informazione "Guglielmo Marconi" (DEI), Cesena, Italy.

F. Quitin is with the School of Electrical and Electronic Engineering, Nanyang Technological University, Singapore.

C. Oestges is with ICTEAM Institute, Electrical Engineering Department, Université catholique de Louvain, Louvain la Neuve, Belgium.

Color versions of one or more of the figures in this communication are available online at http://ieeexplore.ieee.org.

Digital Object Identifier 10.1109/TAP.2014.2322901